Nanoscale

PAPER

View Article Online
View Journal | View Issue

Cite this: *Nanoscale*, 2024, **16**, 7437

First-principles study of the oxidation susceptibility of WS_2, WSe_2, and WTe_2 monolayers†

Ashima Rawat,*[a] Lokanath Patra,[b] Ravindra Pandey [a] and Shashi P. Karna*[c]

The environmental stability of two-dimensional (2D) transition metal dichalcogenide monolayers is of great importance for their applications in electronic, photonic, and energy storage devices. In this study, we focus on understanding the susceptibility of WS_2, WSe_2, and WTe_2 monolayers to oxygen exposure in the form of atomic oxygen and O_2 and O_3 molecules, respectively. Calculations based on the van der Waals-corrected density functional theory predicted that O_2 and O_3 molecules are weakly adsorbed on these monolayers, although atomic oxygen prefers chemisorption accompanied by a significant charge transfer from the surface to oxygen. In the physisorbed molecular configurations consisting of O_2 and O_3, the partially oxidized monolayers retain their geometrical and electronic structures. The calculated transition path as the oxygen approaches the surface shows a high-energy barrier for all cases, thus explaining the photo-induced formation of the oxidized configurations in the experiments. Furthermore, oxidizing the WS_2 monolayer is predicted to modify its electronic structure, reducing the band gap with increasing oxygen coverage on the surface. Overall, the calculated results predict the resilience of WS_2, WSe_2, and WTe_2 monolayers against oxygen exposure, thus ensuring stability for devices fabricated with these monolayers.

Received 29th November 2023,
Accepted 13th March 2024

DOI: 10.1039/d3nr06089f

rsc.li/nanoscale

1. Introduction

Two-dimensional (2D) semiconductors, especially transition metal dichalcogenides (TMDs), such as WX_2 and MoX_2 (X: S, Se, Te), have emerged as an attractive class of materials for a wide range of applications in electronics and optoelectronics devices because of their unique electronic properties, such as high carrier mobility, tunable band gap, and anisotropic electron transport.[1–11] However, their device applications also encounter challenges due to their enhanced susceptibility to oxidation under ambient conditions. This rather undesirable chemical property has drawn considerable attention in understanding the stability and oxidation behavior of TMDCs, especially WS_2 and MoS_2.[12–15] In a recent study of thermal stability, Rahman *et al.*[16] found that the monolayer MoS_2 is quite stable up to a temperature of 1300 K against oxidation. However, at 1400 K, oxidation initiation begins, and by 1500 K, MoS_2 readily reacts with O_2. Another study by Zhao *et al.* delved into O_2 adsorption on both pristine and defective TMD monolayers. The research highlighted the inert nature of defect-free TMDs to O_2, while oxidation, an exothermic process, primarily occurred at chalcogen vacancies with adsorption energies ranging from 1.8 to 3.9 eV.[17] Investigations on bilayer MoS_2 demonstrated a substantial reduction in the "ON" state current under ambient conditions. The reduced current was attributed to additional scattering centers from chemisorption on defect sites, indicating the sensitivity of TMDs to ambient conditions and the impact on electronic properties.[18] For the case of WS_2, a recent experimental study has demonstrated its oxidation under exposure to UV light, but this photo-oxidation of WS_2 is not fully understood.[19] These studies collectively provide an enhanced understanding of the susceptibility of TMDs toward oxidation and its implications on device performance. However, this understanding also raises the following questions: (1) What is the mechanism of oxidation of TMDs? (2) What kind of oxidative species are more effective in oxidizing TMDs, thereby affecting the electronic band structure and other electronic properties? To address these questions, we have systematically studied the reaction of three oxidizing species, namely free O atoms and

[a]*Department of Physics, Michigan Technological University, Houghton, MI, 49931, USA. E-mail: arawat2@mtu.edu*
[b]*Department of Mechanical Engineering, University of California, Santa Barbara, Santa Barbara, CA 93106-5070, USA*
[c]*DEVCOM Army Research Laboratory, Weapons, and Materials Research Directorate, ATTN: FCDD-RLW, Aberdeen Proving Ground, Aberdeen, Maryland 21005-5069, USA. E-mail: shashi.p.karna.civ@army.mil*

†Electronic supplementary information (ESI) available. See DOI: https://doi.org/10.1039/d3nr06089f

O_2 and O_3 molecules with WS_2, WSe_2, and WTe_2 within the framework of density functional theory (DFT) and climbing image nudged elastic band (CINEB) methods. Our emphasis will be on understanding the effects on geometrical and electronic structures and trying to develop a detailed understanding of the oxidation process in terms of chemical bonding, dissociation energy, and density of states in the current study.

2. Computational method

DFT-based calculations using the projected augmented wave (PAW) pseudopotential[20] were performed as implemented in the Vienna *ab initio* simulation package (VASP).[21–24] The Perdew–Burke–Ernzerhof form of the generalized gradient approximation (PBE-GGA)[25] was used, along with the van der Waals (vdW) correction term (D3) proposed by Grimme.[26] The convergence criteria for energy and the Hellmann–Feynman force acting on each atom were set to 10^{-6} eV and 0.01 eV $Å^{-1}$, respectively. The Brillouin zone was sampled using a centered *k*-point grid of size (12 × 12 × 1). A (2 × 2 × 1) periodic supercell was constructed for the monolayers, and periodic image interactions were minimized by using a vacuum of 15 Å along the *z*-axis direction. The dynamic stability of the system was determined by calculating the phonon frequencies using the PHONOPY package,[27,28] for which the force constants were obtained using density functional perturbation theory.[29]

The oxygen adsorption energy ($E_{adsorption}$) was calculated using the following expression.[30–34]

$$E_{adsorption} = E_{(oxygen+WX_2)} - (E_{(WX_2)} + E_{(oxygen)}) \quad (1)$$

where $E_{(oxygen+WX_2)}$ is the total energy of the adsorbed configuration, $E_{(WX_2)}$ is the total energy of the pristine monolayer, and $E_{(oxygen)}$ is the total energy of an oxygen (atomic oxygen or O_2 or O_3 molecule).

The CINEB method,[35] as implemented in VASP, was employed to calculate the minimum energy paths describing the interaction between an oxygenous species, atomic oxygen, and O_2 and O_3 molecules, respectively, and a TMD monolayer. The CINEB method generates a set of six intermediate configurations (*i.e.*, images) from the predetermined initial and final configurations. The initial (non-interacting) configuration consists of a molecule about 4.5 Å above the surface for these calculations. The final configuration consists of dissociated oxygens (atomic oxygen or O_2 or O_3 molecule) adsorbed on the monolayer.[36]

3. Results and discussion

Fig. 1 shows the hexagonal (2 × 2) supercell considered for the calculations. For the pristine WS_2, WSe_2, and WTe_2 monolayers, the calculated lattice constants and band gaps are presented in Table 1 and the band structures are provided in Fig. S1, (ESI†) which are in good agreement with the previously reported DFT values. Table S1 (ESI†) lists the structural properties of O_2 and O_3 molecules calculated at the DFT (GGA) level of theory and are reasonably in good agreement with reported theoretical and experimental values: O_2: 1.24 Å (DFT)[41] and 1.21 Å (experiment)[42] and O_3: 1.28 Å (DFT[43] and experiment[44]), 116.49° (experiment)[43] and 117.90° (DFT).[44]

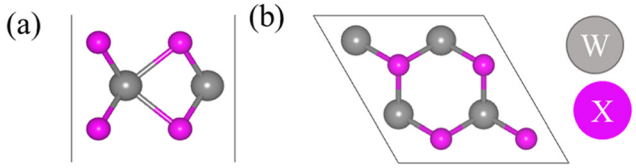

Fig. 1 (a) Side and (b) top views of the pristine WS_2, WSe_2, and WTe_2 monolayers. Color codes: gray: W and pink: chalcogen (S/Se/Te).

Table 1 Lattice parameters and band gaps for WX_2 monolayers calculated at the PBE-DFT level of theory

Monolayers	$a = b$ (Å)	Band gap (eV)
WS_2	3.18 (3.18[37,38])	1.86 (1.81[37,38])
WSe_2	3.31 (3.31[37], 3.32[39,40])	1.57 (1.55[37], 1.53[40])
WTe_2	3.56 (3.56[37])	1.08 (1.02[37])

The equilibrium configurations of the oxygen adsorbed on WS_2, WSe_2, and WTe_2 monolayers are shown in Fig. 2. Three different surface sites were considered for adsorption calculations: $(chalcogen)_{top}$, W_{top}, and hollow. Interestingly, the energetically preferred sites, shown in Fig. 2, consist of an O atom forming a bond with the chalcogen atom (*i.e.*, the $(chalcogen)_{top}$ site). The remaining O atoms in O_2 and O_3 are slightly elongated parallel to the surface approaching the neighboring chalcogen atom. Table 2 lists the adsorption energy (E_{adsorb}), dissociation energy (E_{diss}), molecule–surface distance (R_{X-O}), charge transferred from the surface to molecule (Q_o), and activation barrier height ($E_{barrier}$), describing the interaction of O, O_2, and O_3 with the WS_2, WSe_2, and WTe_2 monolayers. Note that the dissociation energy (E_{diss}) was calculated as the difference between the total energy of the dissociated configuration (*i.e.*, $O_2 \rightarrow O + O$ or $O_3 \rightarrow O + O + O$) and the non-interacting configuration consisting of a molecule of about 4.5 Å above the surface.[36]

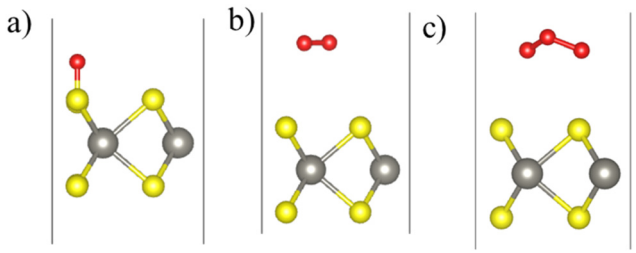

Fig. 2 Calculated equilibrium configurations of (a) O, (b) O_2, and (c) O_3 molecules adsorbed on the WS_2 monolayer. Color code: S (yellow), W (gray), and O (red).

Table 2 WS_2, WSe_2, and WTe_2 monolayers interacting with O, O_2, and O_3: the calculated adsorption energy per oxygen atom (E_{adsorb}), dissociation energy (E_{diss}), molecule–surface distance (R_{X-O}), charge transferred from the surface to molecule (Q_o), and the energy barrier height for dissociation ($E_{barrier}$)

	Monolayer		WS_2	WSe_2	WTe_2
O	Chemisorption	E_{adsorb}, eV per atom	−3.92	−3.00	−3.44
		R_{x-o}, Å	1.48	1.65	1.85
		Q_0/O atom	1.91*e*	0.86*e*	0.98*e*
O_2	Physisorption	E_{adsorb}, eV per atom	−0.05	−0.03	−0.16
		R_{x-o}, Å	3.39	3.59	3.67
		Q_0/O atom	≈0.0*e*	0.03*e*	0.08*e*
	Dissociation	E_{diss}, eV	−0.96	1.23	0.28
		R_{x-o}, Å	1.48	1.65	1.82
		Q_0/O atom	1.9*e*	0.81*e*	1.08*e*
		$E_{barrier}$, eV	5.47	5.17	5.05
O_3	Physisorption	E_{adsorb}, eV per atom	−0.07	−0.08	−0.14
		R_{x-o}, Å	3.05	2.95	2.93
		Q_0/O atom	0.06*e*	0.15*e*	0.22*e*
	Dissociation	E_{diss}, eV	−1.43	1.04	≈0
		R_{x-o} (Å)	1.48	1.65	1.82
		Q_0/O atom	1.88*e*	0.58*e*	0.77*e*
		$E_{barrier}$, eV	6.03	7.30	6.85

Atomic oxygen interacting with the WS_2, WSe_2, and WTe_2 monolayers tends to chemisorb itself onto the top of the chalcogen atom (*i.e.*, S or Se or Te) with an equilibrium bond distance, R_{x-o}, of 1.48, 1.65, and 1.85 Å for WS_2, WSe_2, and WTe_2, respectively. The calculated E_{adsorb} is −3.92, −3.0, and −3.44 eV for WS_2, WSe_2, and WTe_2, respectively. We note that atomic oxygen forms an ionic-covalent bond with an S atom of WS_2 as in the SO molecule for which R_{S-O} is 1.48 Å.[45] The bonding follows a relatively large charge transfer (1.91e) from the monolayer (S) to atomic O, thereby resulting in chemisorption on the surface. A lesser degree of ionicity is predicted for the Se–O and Te–O bonds for the chemisorbed complexes on the WSe_2 and WTe_2 monolayers. In the context of monolayers composed of WX_2, the interaction between tungsten (W) and chalcogen (X) atoms is characterized by a reduction in the charge transfer from W to X, *i.e.* ΔQ = 1.31e, 0.56e, and 0.11e for WS_2, WSe_2, and WTe_2, respectively.[46] Hence the affinity of oxygen for forming a bond with S is much higher than those for Se and Te since S has more charge than Se/Te. Furthermore, an inspection of the partial density of states (Fig. S2, ESI†) shows that chemisorption of atomic oxygen does not induce gap states in the band gaps of the WS_2, WSe_2, and WTe_2 monolayers.

In contrast to the atomic oxygen chalcogenide interaction, the O_2 and O_3 molecules prefer a weakly physisorbed configuration on top of the WS_2, WSe_2, and WTe_2 monolayers with much lower E_{adsorb} in the range of 0.03–0.16 eV with the corresponding bond distance, R_{x-o}, of about ≈3 Å or greater in their equilibrium configurations (Table 2).

This contrasting nature of adsorption can be attributed to the strong O–O bond(s) with bond dissociation energies of 5.11 and 6.27 eV in O_2 and O_3 molecules, respectively,[47] which prevents a strong interaction with surface chalcogen atoms of the WS_2, WSe_2, and WTe_2 monolayers. To assess the feasibility of charge transfer from the surface to the molecules, we have compared the relative positions of the Fermi levels of the monolayers with the lowest unoccupied molecular levels (LUMO) of the $O/O_2/O_3$ molecules.[36,48] From Fig. 3, we note that for the WSe_2 and WTe_2 monolayers, the Fermi levels lie above the O, O_2, and O_3 levels, whereas for WS_2, the Fermi level straddles only the O and O_3 levels. We can, thus, expect finite charge transfer in all the adsorption cases except for the O_2 on the WS_2 monolayer. We quantified this charge transfer using Bader charge analysis as presented in Table 2, which confirms that there is almost no charge transfer in the case of O_2 physisorbed on the WS_2 monolayer, as displayed in Fig. 3. It is worth noting that in the weakly physisorbed configurations, both O_2 and O_3 retain their structural identity in terms of the bond length and bond angles: R(O–O) is 1.24 Å for the O_2 complexes, and (R(O–O), A(O–O–O)) are (1.29 Å, 117.5°), (1.30 Å, 117.0°), and (1.31 Å, 116.3°) for the O_3-WS_2, O_3-WSe_2, and O_3-WTe_2 complexes, respectively. The calculated R(O–O) values for isolated O_2 and O_3 molecules are 1.24 Å and 1.28 Å, respectively. Note that the adsorption energy of the O_2 molecule for the pristine MoS_2 was reported to be 58 meV.[49]

Next, we calculated the transition path taken by both O_2 and O_3 molecules approaching the surface using the CINEB method, as displayed in Fig. 4. Here, the initial (non-interacting) configuration consisted of a molecule placed at ~4.5 Å above the monolayer, and the final configuration consisted of the dissociated atomic oxygen, forming bonds with the surface atoms (*i.e.*, S or Se or Te) of the monolayers.

The calculated molecular transition path exhibits a relatively high energy barrier for either O_2 or O_3 dissociation on these monolayers. The energy barrier for O_2 dissociation to atomic oxygens is calculated to be ≈5 eV, whereas that for O_3 dissociation to atomic oxygens is predicted to be ≥6 eV (Table 2). Notably, among the investigated monolayers, only the WS_2 monolayer preferred the oxidized configurations with an $E_{dissociation}$ ≈−0.96 eV for O_2 and −1.43 eV for O_3 relative to

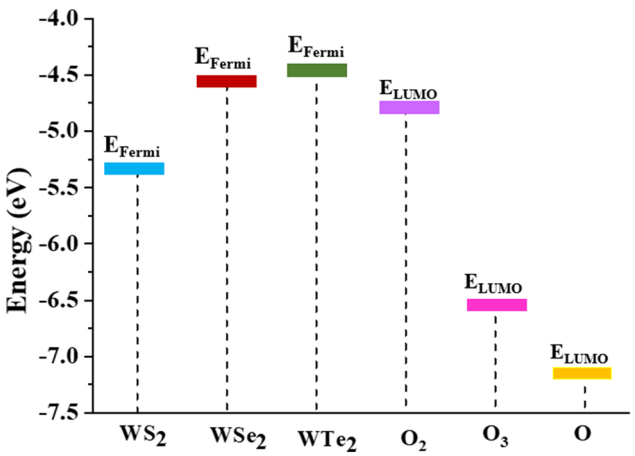

Fig. 3 Schematic diagram displaying the monolayer's Fermi level (E_{Fermi}) and the lowest unoccupied molecular orbital (E_{LUMO}) of atomic O and molecular O_2 and O_3.

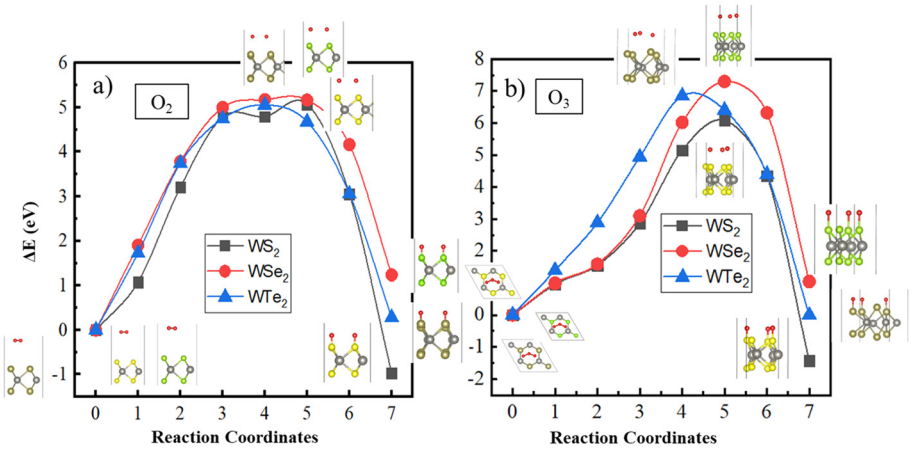

Fig. 4 Molecular transition path on the WS_2, WSe_2, and WTe_2 monolayers for (a) O_2 and (b) O_3 molecules calculated using the CINEB method.

the non-interacting configurations. This can be attributed to the ease with which S–O bonds can form on the WS_2 monolayer relative to the Se–O or Te–O surface bonds for the other monolayers. The oxidized WSe_2 or WTe_2 monolayers are not predicted to be energetically preferred (Table 2). It should be noted that experiments have been performed on the diatomic molecules SO, SeO, and TeO, reporting their vibrational properties.[50]

After recognizing that a partially oxidized WS_2 monolayer (with 25% surface coverage) can be stable, we now examine the electronic properties and the stability of the fully oxidized WS_2 monolayer (with 100% surface coverage).

In the equilibrium configuration of the oxidized WS_2 monolayer, the calculated S–O bond length is 1.48 Å, similar to that predicted for a partially oxidized WS_2 surface (Table 2). Another striking feature appears in the calculated total density of states at the Fermi level for the oxidized WS_2 monolayer, as shown in Fig. 5. By comparing the pristine WS_2 (Fig. 5a) with the partially oxidized one (Fig. 5b), we observed that the band gap reduces by 0.36 eV, and as we move away from the Fermi level in the valence states, new hybridized S–O states appear due to the formation of S–O bonds. A similar observation has been made for SnS/SnSe/GeS/GeSe monolayers where oxygen chemisorption leads to band gap reduction with the activation barrier O_2 in the range from 1.26 to 1.60 eV.[51] Notably, these studies did not address the oxidation of the monolayers by atomic O and O_3 molecules.

Further comparison with the fully oxidized monolayer (Fig. 5a) shows that the band gap reduces from 1.86 eV (pristine) to 1.50 eV (Fig. 5b) for the partially oxidized and to 0.30 eV for the fully oxidized WS_2 monolayer and the hybridized states appear near the Fermi level due to the increase in the S–O bonds. In the case of a partially oxidized WS_2 monolayer (Fig. 5b), the upper valence band (width of 6 eV) consists of the dominating S–O bonds with small contributions from W–O bonds. In the fully oxidized monolayer, however, the upper valence band splits into two parts; the S–O band has moved down to about 4 eV relative to the Fermi level as can be seen in Fig. 5c. The reduction in the band gap in TMDs with oxidation has also been previously reported by DFT calculations.[52]

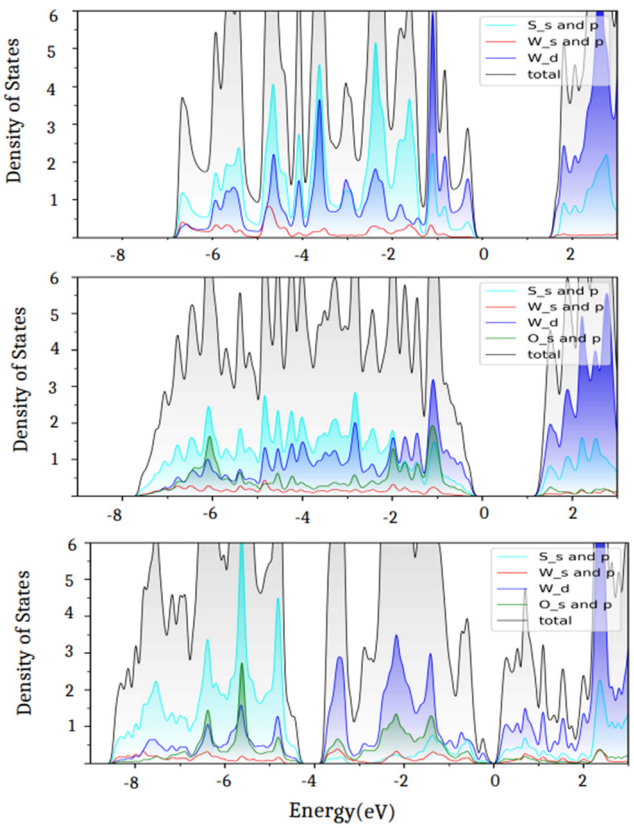

Fig. 5 Projected densities of states for the (a) pristine, (b) partially oxidized, and (c) fully oxidized WS_2 monolayers.

To assess the dynamic stability of the fully oxidized WS_2, phonon dispersion calculations were performed using the PHONOPY package. Fig. 6b displays the calculated phonon dispersion relationship, in which a small pocket of negative frequencies (<0.25 THz) near Γ along the Γ–M direction in the Brillouin zone is noticed. We believe that this small pocket of negative frequencies is an artifact of the technical details such as the supercell size and functional used[53] in the present

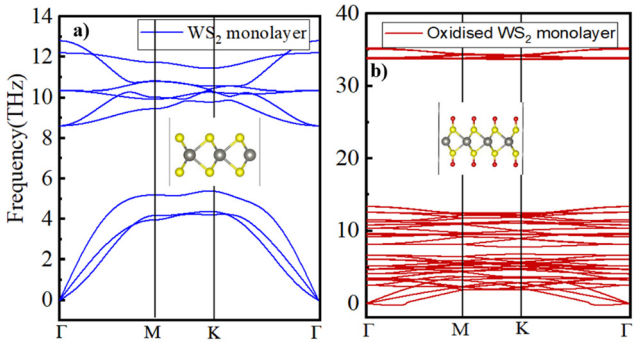

Fig. 6 Calculated phonon dispersion curves for the (a) pristine and (b) oxidized WS_2 monolayers.

study. Otherwise, the calculated phonon band structure for the pristine WS_2 monolayer (displayed in Fig. 6a) is in good accordance with the earlier published reports.[54] A comparison of the phonon band structures of the oxidized WS_2 monolayer with the pristine one clearly shows a distinct phonon branch appearing at approximately 33 THz, which typically corresponds to the S–O bond stretching frequency.[55]

4. Summary

The oxidation susceptibility/resistance of WS_2, WSe_2, and WTe_2 monolayers was investigated from their interaction with atomic oxygen and O_2 and O_3 molecules, respectively. Calculations using van der Waals-corrected density functional theory (DFT) predicted the strongly chemisorbed O in the case of interaction with atomic oxygen, but weakly physisorbed O_2 and O_3 on the monolayer surface. These results are in accordance with a significant charge transfer from the surface to atomic oxygen for all the cases. The weakly physisorbed O_2 and O_3 molecules retain their molecular configurations at about 3.0 Å or more above the surface. The CINEB calculations predicted a large energy barrier for either O_2 or O_3 to dissociate into atomic oxygens on the surface. Interestingly, the oxidized WS_2 is energetically preferred over the pristine WS_2, although the energy barrier is about 5.5 eV, which explains the experimental observation of the high resistance of WS_2 to ambient oxidation for up to ten months but is susceptible to photo-induced oxidation.

Conflicts of interest

There are no conflicts to declare.

Acknowledgements

The authors would like to thank the computational facilities provided by Michigan Technological University. The funding from the Army Research Office through grant no. W911NF-14-2-0088 for partial support of this research at Michigan Tech University (R. P.) is gratefully acknowledged.

References

1 M. Chhowalla, H. S. Shin, G. Eda, L. J. Li, K. P. Loh and H. Zhang, *Nat. Chem.*, 2013, **5**, 263–275.
2 Y. Guo, C. Liu, Q. Yin, C. Wei, S. Lin, T. B. Hoffman, Y. Zhao, J. H. Edgar, Q. Chen, S. P. Lau, J. Dai, H. Yao, H.-S. P. Wong and Y. Chai, *ACS Nano*, 2016, **10**, 8980–8988.
3 G. R. Bhimanapati, Z. Lin, V. Meunier, Y. Jung, J. Cha, S. Das, D. Xiao, Y. Son, M. S. Strano and V. R. Cooper, *ACS Nano*, 2015, **9**, 11509–11539.
4 Z. Wang and B. Mi, *Environ. Sci. Technol.*, 2017, **51**, 8229–8244.
5 E. Singh, K. S. Kim, G. Y. Yeom and H. S. Nalwa, *ACS Appl. Mater. Interfaces*, 2017, **9**, 3223–3245.
6 Y. Wu, N. Joshi, S. Zhao, H. Long, L. Zhou, G. Ma, B. Peng, O. N. Oliveira Jr., A. Zettl and L. Lin, *Appl. Surf. Sci.*, 2020, **529**, 147110.
7 X. Chen, C. Liu and S. Mao, *Nano-Micro Lett.*, 2020, **12**, 1–24.
8 S. Kuriakose, T. Ahmed, S. Balendhran, V. Bansal, S. Sriram, M. Bhaskaran and S. Walia, *2D Mater.*, 2018, **5**, 032001.
9 Q. H. Wang, K. Kalantar-Zadeh, A. Kis, J. N. Coleman and M. S. Strano, *Nat. Nanotechnol.*, 2012, **7**, 699–712.
10 B. Radisavljevic, A. Radenovic, J. Brivio, V. Giacometti and A. Kis, *Nat. Nanotechnol.*, 2011, **6**, 147–150.
11 X.-L. Fan, Y. Yang, P. Xiao and W.-M. Lau, *J. Mater. Chem. A*, 2014, **2**, 20545–20551.
12 J. O. Island, G. A. Steele, H. S. J. van der Zant and A. Castellanos-Gomez, *2D Mater.*, 2015, **2**, 011002.
13 G. Wang, W. J. Slough, R. Pandey and S. P. Karna, *2D Mater.*, 2016, **3**, 025011.
14 Q. Zhao, R. Frisenda, P. Gant, D. Perez de Lara, C. Munuera, M. Garcia-Hernandez, Y. Niu, T. Wang, W. Jie and A. Castellanos-Gomez, *Adv. Funct. Mater.*, 2018, **28**, 1805304.
15 B. Chamlagain and S. I. Khondaker, *ACS Omega*, 2021, **6**, 24075–24081.
16 M. H. Rahman, E. H. Chowdhury and S. Hong, *Surf. Interfaces*, 2021, **26**, 101371.
17 H. Liu, N. Han and J. Zhao, *RSC Adv.*, 2015, **5**, 17572–17581.
18 H. Qiu, L. Pan, Z. Yao, J. Li, Y. Shi and X. Wang, *Appl. Phys. Lett.*, 2012, **100**, 123104.
19 J. C. Kotsakidis, Q. Zhang, A. L. Vazquez de Parga, M. Currie, K. Helmerson, D. K. Gaskill and M. S. Fuhrer, *Nano Lett.*, 2019, **19**, 5205–5215.
20 P. E. Blöchl, *Phys. Rev. B: Condens. Matter Mater. Phys.*, 1994, **50**, 17953.
21 G. Kresse and J. Furthmüller, *Phys. Rev. B: Condens. Matter Mater. Phys.*, 1996, **54**, 11169.

22 G. Kresse and J. Hafner, *Phys. Rev. B: Condens. Matter Mater. Phys.*, 1993, **47**, 558.
23 G. Kresse and J. Hafner, *Phys. Rev. B: Condens. Matter Mater. Phys.*, 1994, **49**, 14251.
24 G. Kresse and J. Furthmüller, *Comput. Mater. Sci.*, 1996, **6**, 15–50.
25 J. P. Perdew, K. Burke and M. Ernzerhof, *Phys. Rev. Lett.*, 1996, **77**, 3865.
26 S. Grimme, S. Ehrlich and L. Goerigk, *J. Comput. Chem.*, 2011, **32**, 1456–1465.
27 A. Togo, F. Oba and I. Tanaka, *Phys. Rev. B: Condens. Matter Mater. Phys.*, 2008, **78**, 134106.
28 A. Togo and I. Tanaka, *Scr. Mater.*, 2015, **108**, 1–5.
29 S. Baroni, S. De Gironcoli, A. Dal Corso and P. Giannozzi, *Rev. Mod. Phys.*, 2001, **73**, 515.
30 A. Zaman, R. Shahriar, S. T. Hossain, M. R. Akhond, H. T. Mumu and A. Sharif, *RSC Adv.*, 2023, **13**, 23558–23569.
31 M. A. Islam, H. Li, S. Moon, S. S. Han, H.-S. Chung, J. Ma, C. Yoo, T. J. Ko, K. H. Oh, Y. Jung and Y. Jung, *ACS Appl. Mater. Interfaces*, 2020, **12**, 53174–55318.
32 T. Liu, Y. Chen, M. Zhang, L. Yuan, C. Zhang, J. Wang and J. Fan, *AIP Adv.*, 2017, **7**, 125007.
33 D. Bahamon, M. Khalil, A. Belabbes, Y. Alwahedi, L. F. Vega and K. Polychronopoulou, *RSC Adv.*, 2021, **11**, 2947–2957.
34 H. Wei, Y. Gui, J. Kang, W. Wang and C. Tang, *Nanomaterials*, 2018, **8**, 646.
35 G. Henkelman, B. P. Uberuaga and H. Jónsson, *J. Chem. Phys*, 2000, **113**, 9901–9904.
36 L. Patra, G. Mallick, R. Pandey and S. P. Karna, *Appl. Surf. Sci.*, 2022, **588**, 152940.
37 A. Rawat, N. Jena and A. De Sarkar, *J. Mater. Chem. A*, 2018, **6**, 8693–8704.
38 Y. Ma, Y. Dai, M. Guo, C. Niu, J. Lu and B. Huang, *Phys. Chem. Chem. Phys.*, 2011, **13**, 15546–15553.
39 D. Le, A. Barinov, E. Preciado, M. Isarraraz, I. Tanabe, T. Komesu, C. Troha, L. Bartels, T. S. Rahman and P. A. Dowben, *J. Phys.: Condens. Matter*, 2015, **27**, 182201.
40 P. Manchanda and R. Skomski, *J. Phys.: Condens. Matter*, 2016, **28**, 064002.
41 A. Panchenko, M. T. M. Koper, T. E. Shubina, S. J. Mitchell and E. Roduner, *J. Electrochem. Soc.*, 2004, **151**, A2016–A2027.
42 H. Nakatsuji and H. Nakai, *Chem. Phys. Lett.*, 1992, **197**, 339.
43 R. Trambarulo, S. N. Ghosh, C. A. Burrus Jr. and W. Gordy, *J. Chem. Phys.*, 1953, **21**, 851–855.
44 D. Farmanzadeh and N. A. Ardehjani, *Appl. Surf. Sci.*, 2018, **444**, 642–649.
45 N. N. Greenwood and A. Earnshaw, *Chemistry of the Elements*, Elsevier, 2012.
46 J. Li, N. V. Medhekar and V. B. Shenoy, *J. Phys. Chem. C*, 2013, **117**, 15842–15848.
47 B. W. Pfennig, *Principles of Inorganic Chemistry*, John Wiley & Sons, 2021.
48 R. L. Anderson, *IBM J. Res. Dev.*, 1960, **4**, 283–287.
49 H. Liu, N. Han and J. Zhao, *RSC Adv.*, 2015, **5**, 17572–11758.
50 P. Haranath, P. T. Rao and V. Sivaramamurty, *Zeitschrift für Physik A*, 1959, **155**, 507–517.
51 Y. Guo, S. Zhou, Y. Bai and J. Zhao, *ACS Appl. Mater. Interfaces*, 2017, **9**, 12013–12020.
52 K. Iordanidou, M. Houssa, G. Pourtois, V. V. Afanas'ev and A. Stesmans, *Phys. Status Solidi RRL*, 2016, **11**, 787–791.
53 V. Zólyomi, N. D. Drummond and V. I. Fal'ko, *Phys. Rev. B: Condens. Matter Mater. Phys.*, 2014, **89**, 205416.
54 A. Berkdemir, H. R. Gutiérrez, A. R. Botello-Méndez, N. Perea-López, A. L. Elías, C.-I. Chia, B. Wang, V. H. Crespi, F. López-Urías, J.-C. Charlier, H. Terrones and M. Terrones, *Sci. Rep.*, 2013, **3**, 1755.
55 K. I. Oh and C. R. Baiz, *J. Chem. Phys.*, 2019, **151**(23), 234107.

